THE JOURNAL OF PHYSICAL CHEMISTRY C

Article

Cite This: J. Phys. Chem. C 2019, 123, 2019−2030

pubs.acs.org/JPCC

Dynamics of Hydride Ions in Metal Hydride-Reduced $BaTiO_3$ Samples Investigated with Quasielastic Neutron Scattering

Carin Eklöf-Österberg,[†] Reji Nedumkandathil,[‡] Ulrich Häussermann,[‡] Aleksander Jaworski,[‡] Andrew J. Pell,[‡] Madhusudan Tyagi,[§,∥] Niina H. Jalarvo,[⊥] Bernhard Frick,[#] Antonio Faraone,[§] and Maths Karlsson*[,†]

[†]Department of Chemistry and Chemical Engineering, Chalmers University of Technology, Göteborg SE-412 96, Sweden

[‡]Department of Materials and Environmental Chemistry, Stockholm University, Stockholm SE-10691, Sweden

[§]National Institute of Standards and Technology, NIST Center for Neutron Research, 100 Bureau Drive, Gaithersburg, Maryland 20899-6102, United States

[∥]Department of Materials Science and Engineering, University of Maryland, College Park, Maryland 20742, United States

[⊥]Chemical and Engineering Materials Division, Oak Ridge National Laboratory, Oak Ridge, Tennessee 37831-6475, United States

[#]Institut Laue-Langevin, 71, Avenue des Martyrs, Grenoble 38000, France

Supporting Information

ABSTRACT: Perovskite-type oxyhydrides, $BaTiO_{3-x}H_x$, have been recently shown to exhibit hydride-ion (H^-) conductivity at elevated temperatures, but the underlying mechanism of hydride-ion conduction and how it depends on temperature and oxygen vacancy concentration remains unclear. Here, we investigate, through the use of quasielastic neutron scattering techniques, the nature of the hydride-ion dynamics in three metal hydride-reduced $BaTiO_3$ samples that are characterized by the simultaneous presence of hydride ions and oxygen vacancies. Measurements of elastic fixed window scans upon heating reveal the presence of quasielastic scattering due to hydride-ion dynamics for temperatures above ca. 200 K. Analyses of quasielastic spectra measured at low (225 and 250 K) and high (400−700 K) temperature show that the dynamics can be adequately described by established models of jump diffusion. At low temperature, ≤250 K, all of the models feature a characteristic jump distance of about 2.8 Å, thus of the order of the distance between neighboring oxygen atoms or oxygen vacancies of the perovskite lattice and a mean residence time between successive jumps of the order of 0.1 ns. At higher temperatures, >400 K, the jump distance increases to about 4 Å, thus of the order of the distance between next-nearest neighboring oxygen atoms or oxygen vacancies, with a mean residence time of the order of picoseconds. A diffusion constant D was computed from the data measured at low and high temperatures, respectively, and takes on values of about 0.4×10^{-6} cm^{-2} s^{-1} at the lowest applied temperature of 225 K and between ca. 20×10^{-6} and 100×10^{-6} cm^{-2} s^{-1} at temperatures between 400 and 700 K. Activation energies E_a were derived from the measurements at high temperatures and take on values of about 0.1 eV and show a slight increase with increasing oxygen vacancy concentration.

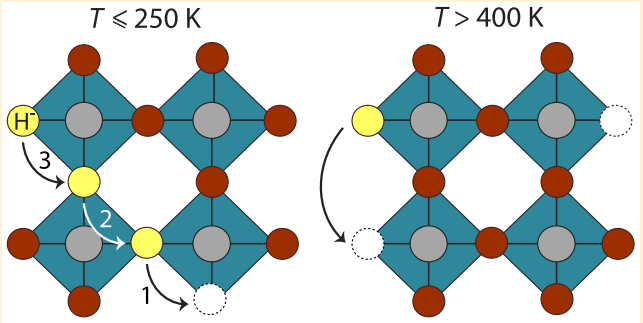

1. INTRODUCTION

Perovskites (ABO_3) can display a wide range of useful properties due to their ability to accommodate different cations, substitution (doping), nonstoichiometry, and structural defects. Of specific concern in this work are transition-metal perovskite oxyhydrides (B = transition metal) in which O^{2-} and H^- ions form commonly the anionic sublattice. Such materials include compounds like $SrVO_2H$[1] and $SrCrO_2H$[2] with unusual magnetic properties, as well as $BaTiO_{3-x}H_x$ ($x < 0.6$)[3] based on the archetypical perovskite $BaTiO_3$ (BTO). In the solid solution, $BaTiO_{3-x}H_x$, O^{2-} and H^- ions form commonly the octahedral environment around Ti, which, accordingly, is in a mixed IV/III oxidation state. In contrast with most other oxyhydrides,[4−10] $BaTiO_{3-x}H_x$ is stable in air up to ca. 400 °C, above which hydrogen gas is released. When present, oxygen is scavenged and $BaTiO_3$ is retained. In inert gas atmospheres containing D_2, a hydride exchange H/D occurs at hydrogen release temperatures. These observations led to the conclusion that the hydride species in $BaTiO_{3-x}H_x$ have to be mobile.

The labile hydride species in $BaTiO_{3-x}H_x$ have not only implications for ion conductivity but also the chemistry of

Received: August 30, 2018
Revised: October 14, 2018
Published: October 31, 2018

DOI: 10.1021/acs.jpcc.8b08451
J. Phys. Chem. C 2019, 123, 2019−2030

$BaTiO_{3-x}H_x$. Kageyama et al.[3] demonstrated that this material represents a versatile precursor toward a range of other mixed anion compounds such as oxynitrides[11−13] and oxyfluorides.[13] Two main possible diffusional routes for the hydride ion in $BaTiO_{3-x}H_x$ have been discussed: (i) vacancy-assisted diffusion and (ii) transformation into a proton and then interstitial diffusion.[3,14−17] Recently, it has been shown by Tang et al.[18] that when x is low ($x < 0.4$), the migration of hydride ions in $BaTiO_{3-x}H_x$ will require the simultaneous movement of oxide ions, which is featured by a relatively high activation energy, of the order of 3.8 eV,[18] whereas when x is high ($x > 0.4$), the concentration of hydride ions is so high that the hydride ions may form a conduction pathway not dependent on the movement of oxygen ions and is then featured by a lower activation energy, of the order of 2 eV.[18] The diffusional motion of the hydride ion can be promoted by introducing oxygen vacancies in the perovskite structure, as demonstrated with $Sr(Ti_{0.95}Sc_{0.05})O_{2.56}H_{0.41}$ for which anion vacancies were created by aliovalent Ti/Sc cation substitution.[19] However, experimental data on the mechanistic aspects of hydride-ion dynamics on an atomic length-scale and how it depends on the concentration of hydride ions and oxygen vacancies and on temperature is lacking.

Interestingly, it has been recently shown that the reduction of $BaTiO_3$ by metal hydrides can yield materials $BaTiO_{3-x}H_y\square_{(x-y)}$ that, similar to $Sr(Ti_{0.95}Sc_{0.05})O_{2.56}H_{0.41}$, contain simultaneously hydridic H and oxygen anion vacancies $\square$.[20] In this work, we investigate the dynamics of hydride ions in three such samples with varying x and y values using quasielastic neutron scattering (QENS) together with powder X-ray diffraction (PXRD), thermal gravimetric analysis (TGA), ^{1}H magic angle spinning (MAS) nuclear magnetic resonance (NMR), and neutron spin-echo (NSE) spectroscopy. Previous QENS reports of oxyhydrides are limited to the study of $LaSrCoO_3H_{0.7}$ by Bridges et al.,[21] who observed hydride-ion mobility characterized by hopping along the direction of vacancies in the hydride-ion sublattice, with a jump distance nearly equivalent to the distance between adjacent hydride-ion sites. It was found that the hopping was initiated in the temperature range used for synthesis of the material (675−725 K) and occurs in conjunction with loss of hydrogen from the sample. The obtained activation energy and hydride-ion diffusion coefficient derived from QENS were E_a = 200−230 meV and $D = (6-10) \times 10^{-5}$ cm^2 s^{-1} in the temperature range of 700−750 K.[21] These data are comparable to data obtained for proton (H^+)-conducting perovskite analogs, such as acceptor-doped barium zirconates, which typically show E_a and D of the order of 100−200 meV and $(1-5) \times 10^{-7}$ cm^2 s^{-1}, respectively, at about 500 K.[22−26] The aim of our study is to determine the dynamical behavior of the hydride ions, as a function of temperature, T, and the concentration of both hydride ions and oxygen vacancies, as well as to compare with the QENS studies of $LaSrCoO_3H_{0.7}$[21] and proton conducting oxides.[22−26]

2. EXPERIMENTAL SECTION

2.1. Sample Preparation. Two reduced $BaTiO_3$ samples, which in the following discussion are termed "CA1" and "CA2", were prepared by mixing powders of $BaTiO_3$ (500 nm particle size, 99.9% purity, ABCR GmbH[27]) and CaH_2 (99.99%, Sigma-Aldrich[27]) in an Ar-filled glovebox in the molar proportion 1:0.3 (that is $BaTiO_3$/H = 1:0.6) and 1:2.25 (that is $BaTiO_3$/H = 1:4.5) for CA1 and CA2, respectively. Approximately 10 g of this mixture was pressed into pellets with a mass of about 1 g (for CA2, a mixture of approximately 10 g was then pressed into one pellet). The pellets were separately placed inside sealed stainless steel ampules (for CA2, the pellet was placed inside one sealed stainless steel ampule) and heated inside an evacuated silica jacket to a temperature of 700 °C for 3 days (for CA2, to a temperature of 600 °C for 2 days). A third sample, "NAB", was prepared by mixing powders of $BaTiO_3$ and $NaBH_4$ (98%, ABCR GmbH[27]) in an Ar-filled glovebox in the molar proportion 1:0.45 (that is $BaTiO_3$/H = 1:1.8). Pellets of this mixture were heated to a temperature of 600 °C for 2 days. The dark-blue colored products (see Figure S1) were washed 3−4 times with a mixture of 0.1 M NH_4Cl and methanol (CA1 and CA2) or 0.1 M hydrochloric acid (NAB) to remove excess metal hydride and the byproducts CaO (CA1 and CA2) and $NaBO_2$ (NAB), respectively. Finally, the CA1, CA2, and NAB samples were dried under dynamic vacuum at 120 °C for about 1 day.

2.2. Powder X-ray Diffraction. PXRD patterns were collected at ambient temperature on a PANalytical X'pert PRO diffractometer operated with Cu Kα_1 radiation and in $\theta-2\theta$ diffraction geometry. Powder samples were mounted on a Si wafer zero-background holder and diffraction patterns measured in a 2θ range 10−90° with 0.013° step size. The Rietveld method, as implemented in the FullProf[28] program, was used for structure and phase analysis.

2.3. Thermal Gravimetric Analysis. Thermal gravimetric analysis (TGA) was carried out using a TA Instruments Discovery system.[27] The samples (≈15 mg powders) were heated in a platinum crucible from room temperature to 900 °C with a heating rate of 5 °C/min. A dry air gas flow of 20 mL/min was applied.

2.4. ^{1}H Magic Angle Spinning Nuclear Magnetic Resonance Spectroscopy. ^{1}H MAS NMR experiments were performed at a magnetic field of 14.1 T (600.12 MHz ^{1}H Larmor frequency) and a MAS rate of 60 kHz on a Bruker Avance-III spectrometer[27] equipped with a 1.3 mm MAS probehead. Acquisitions involved rotor-synchronized, double-adiabatic spin-echo sequence with a 90° excitation pulse of length 1.2 μs, followed by two 50.0 μs tanh/tan short high-power adiabatic pulses[29,30] with 5 MHz frequency sweep.[31] All pulses operated at a nutation frequency of 208 kHz. For each sample, 4096 signal transients with 5 s relaxation delays were accumulated. Shifts were referenced with respect to tetramethylsilane at 0 ppm.

2.5. Quasielastic Neutron Scattering. The QENS experiments were performed on three instruments, i.e., on the IN16B backscattering spectrometer at the Institut Laue-Langevin (ILL),[32,33] on the HFBS backscattering spectrometer at the NIST Center for Neutron Research (NCNR),[34] and on the backscattering spectrometer BASIS at the Spallation Neutron Source (SNS).[35] For the present work, the key differences between the three instruments are that IN16B and HFBS are suitable for elastic fixed window scans (EFWSs) and allow the dynamic structure factor, $S_{meas}(Q, \omega)$, to be measured with higher resolution than that allowed by BASIS, whereas BASIS gives access to a larger dynamic range (cf. ≈20 ps to 2 ns at IN16B and HFBS and ≈2 ps to 0.1 ns at BASIS). Even longer time scale dynamics, from 5 ps up to 15 ns, were measured using the neutron spin-echo (NSE) technique. In comparison to neutron backscattering, NSE gives the intermediate scattering function, $I(Q, t)_{meas}$, rather than $S_{meas}(Q, \omega)$. Additionally, the NSE technique allows the

DOI: 10.1021/acs.jpcc.8b08451
J. Phys. Chem. C 2019, 123, 2019−2030

separation of incoherent and coherent scattering contributions, which can give information about the concentration of the different elements in the studied sample.

The IN16B measurements were performed on CA1.[36] Approximately 10 g of CA1 was thinly distributed inside an aluminum package that was subsequently rolled into a 62 mm long annulus with a diameter of 22 mm. An aluminum can, which was vacuum-sealed using a stainless-steal head that was pinched to the head of the sample cell, was used as sample holder, and a cryofurnace was used to reach the desired temperatures. IN16B was operated with 6.271 Å wavelength neutrons, yielding an energy resolution of 0.75 μeV at full width half-maximum (FWHM) and an accessible momentum transfer (Q) range of 0.1−1.8 Å^{-1}. First, we obtained the EFWSs by examining the intensity in the elastic channel, i.e., at neutron energy transfer $\hbar\omega$ = 0, of the CA1 sample upon heating from base temperature $T \approx$ 2−550 K. By this approach, the onset temperature of diffusive dynamics was gathered. On the basis of this information, scans of the dynamic structure factor, $S_{meas}(Q, \omega)$, were programmed within the dynamic range of ±30 μeV. The measurements of $S_{meas}(Q, \omega)$ were performed at 225, 250, 300, and 360 K, in that order, with a measuring time between 2 and 4 h per spectrum. The measurement of a vanadium standard at 2 K was used as a resolution function in the data analysis and to normalize for the detector efficiency.

The HFBS measurements were performed on NAB and focused on establishing the onset of dynamics by an EFWS over the temperature range from 20 to 475 K. Similar to IN16B, HFBS was operated with 6.27 Å wavelength neutrons, yielding an energy resolution of 0.83 μeV. Approximately 10 g of NAB was thinly distributed inside an aluminum package that was subsequently rolled into an 85 mm long annulus with a diameter of 18 mm. An aluminum can, which was vacuum-sealed using a lead wire, was used as sample holder, and a closed-cycle refrigerator was used to reach the desired temperatures.

The BASIS measurements were performed on CA2 and NAB. The samples, approximately 10 g of CA2 and NAB, respectively, were thinly distributed inside aluminum packages that were subsequently rolled into 54 mm long annuli with a diameter of 29 mm. An aluminum can, which was vacuum-sealed using aluminum foil, was used as a sample holder, and a closed-cycle refrigerator was used to reach the desired temperatures. BASIS analyzes for 6.267 Å, yielding an energy resolution of 3.5 μeV FWHM and an accessible Q range of 0.2−2 Å^{-1}. A hot stick and a heat shield were used to achieve temperature equilibrium at high temperatures. QENS spectra were measured at 30, 400, 500, 600, and 700 K, in that order. The spectrum measured at 30 K was used as the resolution function in the data analysis. The measuring time was 5 h at 30 K and 3−4 h at 400, 500, 600, and 700 K, respectively.

For any of the neutron backscattering experiments, we applied standard corrections to the data comprising empty can scattering, detector efficiency adjustments, and absorptions evaluations. Due to a Bragg peak at approximately Q = 1.57 Å^{-1} and the presence of small-Q scattering due to an ascending small-angle signal related to the powder nature of the samples, some of the data points were removed from the analysis. All QENS spectra were reduced and analyzed using the DAVE[37] software.

2.6. Neutron Spin-Echo Spectroscopy. The NSE measurements were performed at the NCNR[38] on CA2 prior to the BASIS measurement. The sample, approximately 10 g of CA2, was thinly distributed inside an aluminum package that was subsequently rolled into a 50 mm long annulus with a diameter of 30 mm. An aluminum can was used as a sample holder, and a closed-cycle refrigerator was used to reach the desired temperatures. The sample container was partly open during the measurements, and the measurements were performed under vacuum. The NSE data was collected using incident neutrons with an average wavelength of 6 Å and at a Q value of 1.1 Å^{-1}, which gave a dynamic range from 5 ps to 15 ns. Data were measured at temperatures between 300 and 660 K. The measurement of a TiZr alloy at 300 K was used as resolution function in the data analysis.

3. RESULTS

3.1. Structural Characterization Analyses. The results of the structural characterization analyses for CA1, CA2, and NAB are depicted in Figures 1 and 2 and summarized in

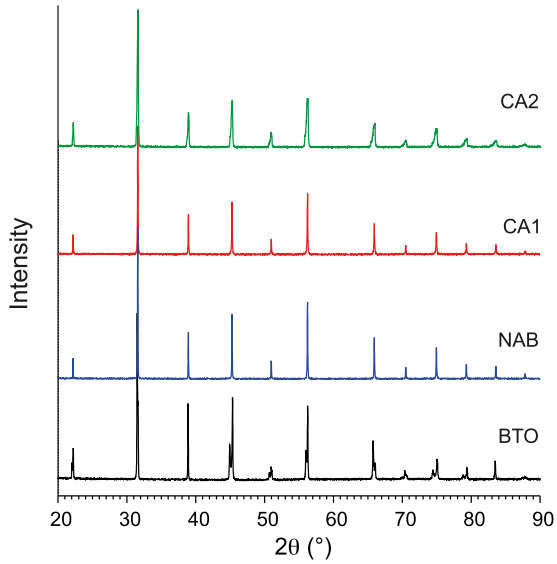

Figure 1. PXRD patters of CA1, CA2, and NAB.

Table 1. The details of the Rietveld refinement can be found in the Supporting Information (Figure S2 and Table S1). In agreement with previous reports, hydride reduction of room-temperature tetragonal $BaTiO_3$ with CaH_2 affords a cubic product (Figure 1). The simple cubic perovskite structure is also obtained when using $NaBH_4$ as reducing agent. Note that the concentration of metal hydride employed in the synthesis of CA1 and NAB ($BaTiO_3$/H = 0.6 and 1.8, respectively) was considerably lower than that applied in the original synthesis[3] of $BaTiO_{3-x}H_x$ affording $BaTiO_{2.38}H_{0.62}$ ($BaTiO_3$/H = 6). The lattice parameter of CA1 and NAB is very similar, 4.0055 and 4.0044 Å, respectively, which is considerably smaller than that reported for $BaTiO_{2.38}H_{0.62}$ (4.0236 Å).[3] For the synthesis of CA2, a higher metal hydride concentration was used ($BaTiO_3$/H = 4.5). The powder pattern of CA2 indicated a heterogeneous product, consisting of two cubic phases (cf. Figure S2). Their lattice parameters (4.012 and 4.029 Å) are significantly larger compared to those of CA1 and NAB. CA1, CA2, and NAB represent anion-deficient oxyhydrides $BaTiO_{3-x}H_y\square_{(x-y)}$. As shown in ref 20, x and y values can be assessed by a combined TGA and ^{1}H MAS NMR analysis (Figure 2).

DOI: 10.1021/acs.jpcc.8b08451
J. Phys. Chem. C 2019, 123, 2019−2030

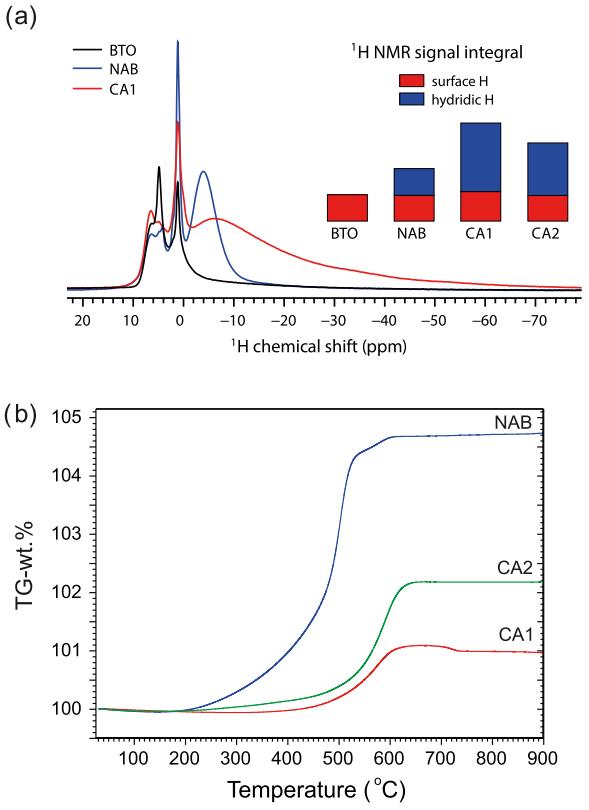

Figure 2. (a) ^{1}H MAS NMR spectra of the precursor material tetragonal $BaTiO_3$ (BTO) and the reduced samples CA1 and NAB (acquired on a 14.1 T spectrometer at 60 kHz MAS). The spectrum of CA2 was acquired on a 9.4 T spectrometer and is shown in Figure S3. The inset shows proton signal integral of all reduced samples with respect to BTO. (b) TGA traces of CA1, CA2, and NAB. The sample CA1 shows a minute weight loss (≈0.1%) above 700°, whose origin is not clear.

Figure 2a shows the ^{1}H MAS NMR spectra. First, the precursor material, tetragonal $BaTiO_3$, displays distinct resonances at 1.1, 4.8, and 6.5 ppm, which are attributed to surface OH species because the spectrum after heating this material to 900 °C, which would remove any structural OH, is virtually identical. When quantifying the H content of the $BaTiO_3$ precursor by relating its ^{1}H NMR signal intensity to that of adamantane ($C_{10}H_{16}$) in the same rotor volume and under identical conditions, one obtains a molar ratio H/$BaTiO_3$ ≈ 0.039. The spectra of NAB, CA1, and CA2 (Figure S3) show additional broad resonance at −4, −8, and −20 ppm, respectively. This is distinct from the precursor, and according to ref 20, the signal is attributed to hydridic H on the O position in the perovskite structure. The large range of negative chemical shifts and breadth of the signals signify metallic conductivity. In addition, there are sharp resonances in the positive 1−7 ppm region, similar to the precursor spectrum, which are, thus, surface OH species. When deconvoluting the ^{1}H signal into a protic (positive ppm) and hydridic (negative ppm) part, one notices that the concentration of protic surface hydroxyl is comparable for the precursor and CA1, CA2, and NAB. Also, deconvolution allows one to estimate the molar ratio between hydridic H and $BaTiO_3$ in the reduced samples to be approximately 0.10, 0.08, and 0.04, respectively. These values will be referred to as y values in the formula $BaTiO_{3-x}H_y\square_{(x-y)}$.

The TGA traces of CA1, CA2, and NAB are shown in Figure 2b. The samples show initially a small weight loss (0.1−0.15%), which is attributed to surface water/hydroxyls. The subsequent weight increase, above 200 °C for NAB and 400 °C for CA1 and CA2, is then due to oxidation. Here, one can consider two border cases: a vacancy-free oxyhydride will oxidize according to $BaTiO_{3-x}H_x + 0.75x\ O_2 \rightarrow BaTiO_3 + 0.5x\ H_2O$, and a hydride-free O-deficient $BaTiO_{3-x}$ will oxidize according to $BaTiO_{3-x} + 0.5x\ O_2 \rightarrow BaTiO_3$. From the weight gains, which will be very similar because of the small mass of H, the x values in the formula $BaTiO_{3-x}H_y\square_{(x-y)}$ can be extracted. CA1 and CA2 attained weight gains, which translate to x = 0.18 and 0.37, respectively. The corresponding value for NAB is very high, x = 0.75. The combined ^{1}H MAS NMR and TGA results (i.e., x and y values) are included in Table 1. For NAB, the concentration of O vacancies exceeds that of hydridic H by an order of magnitude whereas for CA1, the concentration of hydridic H is slightly higher than that of the O vacancies. The heterogeneous nature of CA2 (as suggested from the PXRD pattern) may be due to phase segregation into a O vacancy-rich and H-rich phase. However, this is not supported by the lattice parameters that are both larger compared to those of NAB and CA1 (cf. Table 1). At this point, the heterogeneous nature of CA2 remains unclear.

3.2. Elastic Fixed Window Scans. We report in Figure 3 the EFWSs for CA1 and NAB, which have been normalized to the data point at the lowest temperature (2 and 20 K for CA1 and NAB, respectively).[39,40] As expected, both samples show a drop in the elastic intensity upon heating. For CA1, the intensity evolves from a virtually T-independent behavior below 150 K to a roughly linear decrease between 200 and 320 K, a more rapid decrease between ca. 320 and 360 K, and a

Table 1. Results of the Characterization of CA1, CA2, and NAB as Obtained from XRD, TGA, and NMR[a,b]

sample ID	synthesis conditions	lattice parameter (Å)	x_H from TG	$x_\square$ from TG	y_H from ^{1}H NMR	formula $BaTiO_{3-x}H_y\square_{x-y}$
CA1	$BaTiO_3/CaH_2$ = 1:0.3 ($BaTiO_3$/H = 1:0.6), 700 °C, 3 days	4.0055(2)	0.18	0.17	0.10	x = 0.18 y = 0.1 [H] > [□]
CA2	$BaTiO_3/CaH_2$ = 1:2.25 ($BaTiO_3$/H = 1:4.5), 600 °C, 2 days	I 4.0119(1) 79(2)% II 4.0295 21%	0.37	0.35	0.08	x = 0.35 y = 0.08 [H] < [□]
NAB	$BaTiO_3/NaBH_4$ = 1:0.45 ($BaTiO_3$/H = 1:1.8), 600 °C, 2 days	4.0044(1)	0.75	0.70	0.04	x = 0.7 y = 0.04 [H] ≪ [□]

[a] x_H refers to a reaction $BaTiO_{3-x}H_x + 0.75x\ O_2 \rightarrow BaTiO_3 + 0.5x\ H_2O$. [b] $x_\square$ refers to a reaction $BaTiO_{3-x}H_x + 0.5x\ O_2 \rightarrow BaTiO_3$.

DOI: 10.1021/acs.jpcc.8b08451
J. Phys. Chem. C 2019, 123, 2019−2030

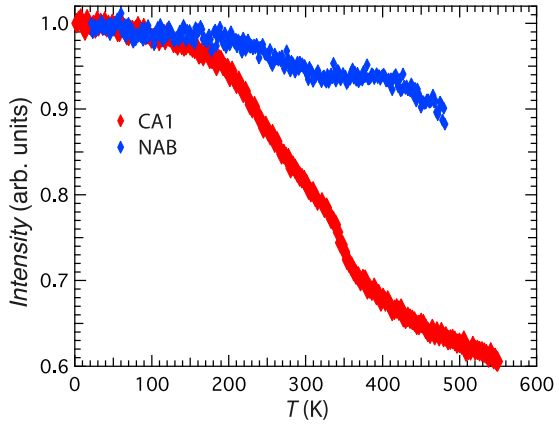

Figure 3. Normalized EFWSs of CA1 and NAB, as measured on IN16B and HFBS, respectively, and summed over the Q range from 0.57 to 1.79 and 0.36 to 1.68 Å^{-1} (excluding Q values at and around 1.57 Å^{-1} due to a Bragg peak) for CA1 and NAB, respectively. Error bars are within the size of the symbols. Throughout the paper and the SI, error bars and uncertainties represent one standard deviation.

leveling off at even higher temperatures. The nonlinear T dependence of the intensity over the investigated T range gives evidence of additional, nonsimple, dynamical processes setting in above ca. 150 K, within the time window accessible by the instrument.[41] The leveling off at the highest temperatures indicates that the observed dynamics becomes too fast to be resolved within the accessible time window of IN16B.

For NAB, the intensity shows a similar T dependence to CA1 up to around 300 K. It is roughly constant between 300 and 400 K and decreases again between 400 and 480 K. We also observe that the decrease of NAB is not as prominent as that of CA1, which probably relates to a lower amount of hydride ions involved in the observed dynamics.

3.3. Quasielastic Spectra at Low Temperatures. CA1 was subjected to QENS measurements at 225, 250, 300, and 360 K on IN16B. The T range in the following is considered "low temperature". Figure 4a shows the measured dynamical structure factor, $S_{meas}(Q, \omega)$, as obtained from the measurement at 225 K, and Q = 1.1 Å^{-1}. The spectra for 225−360 K are shown in Figure S4. The spectra have been fitted to a function composed of an elastic term, $A_0(Q)\delta(\omega)$, a quasielastic component described with a Lorentzian function, $A_1(Q)L_1(Q, \omega)$, and a linear sloping background, $a(Q) + b(Q)\omega$, all convoluted with the resolution function of the instrument, $R(Q, \omega)$, i.e.,

$$S_{meas}(Q, \omega) = [A_0(Q)\delta(\omega) + A_1(Q)L_1(Q, \omega) + a(Q) + b(Q)\omega] \otimes R(Q, \omega) \quad (1)$$

The Lorentzian function can be expressed as

$$L_1(Q, \omega) = \frac{2}{\pi} \frac{\Gamma_1(Q)}{(2\hbar\omega)^2 + \Gamma_1(Q)^2} \quad (2)$$

where $\Gamma_1(Q)$ is the Lorentzian's FWHM. $\Gamma_1(Q)$ relates to a characteristic relaxation (or residence) time, τ_1, according to $\tau_1 = 2\hbar/\Gamma_1$. The Lorentzian thus contains information about both the time- and length-scale dependence of the observed dynamics. The background should be associated with relaxational dynamics too fast to be adequately analyzed with the chosen instrument and, because it is sloping, also to vibrational modes (i.e., inelastic scattering) occurring at energy transfers

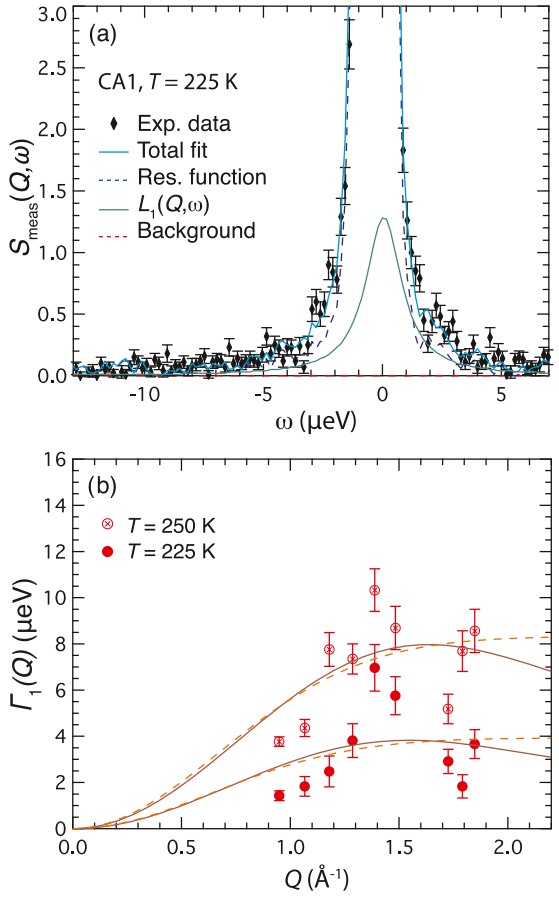

Figure 4. (a) $S_{meas}(Q, \omega)$ of CA1 at Q = 1.1 Å^{-1} and 225 K, as measured on IN16B, together with the best fit according to eq 1. (b) $\Gamma_1(Q)$ of CA1, as extracted from the IN16B data at 225 and 250 K (the data point at Q = 1.6 Å^{-1} has been removed due to interference with a Bragg peak at 1.57 Å^{-1}). The solid lines are fits to a Chudley−Elliott model, and the dashed lines are fits to a Gaussian model.

larger than zero but overlapping (in part) with the quasielastic region. Although, a priori, the quasielastic broadening could, in principle, reflect the dynamics of both oxide and hydride ions, reported values of oxide-ion diffusion in $BaTiO_3$ samples are in the range $\tau = 10^{-5}$ s at T = 700 K,[42] suggesting it is negligible at the picosecond time range as probed here. We thus assign the quasielastic broadening to the hydride ions in the material. Further, since the total neutron scattering cross section of hydrogen is predominantly incoherent (cf. $\sigma_{H(inc.)}$ = 80.3 barns, $\sigma_{H(coh.)}$ = 1.8 barns[43]), largely self-dynamics of the hydride ions are measured.

We show in Figure 4b the quasielastic width $\Gamma_1(Q)$, as extracted from the QENS spectra at 225 and 250 K. $\Gamma_1(Q)$ could not be reliably determined at higher temperatures, 300 and 360 K, because of a too low scattering intensity. For 225 and 250 K, $\Gamma_1(Q)$ can be fitted well by established jump diffusion models. The solid lines in Figure 4b are fits to a Chudley−Elliott model

$$\Gamma_1(Q) = \frac{2\hbar}{\tau}\left(1 - \frac{\sin(QR)}{QR}\right) \quad (3)$$

which considers jumps of a distance R between points on a regular lattice and assumes that each mobile atom has a mean residence time τ, i.e., the average time between successive jumps.[44,45] The jump length, R, is related to the diffusion

DOI: 10.1021/acs.jpcc.8b08451
J. Phys. Chem. C 2019, 123, 2019−2030

Table 2. Results for the Chudley–Elliott Model and the Gaussian Model, as Obtained from the Fitting to the IN16B and BASIS Data

		Chudley–Elliott model			Gaussian model		
Sample	T (K)	R (Å)	τ (ps)	D (10^{-6} cm^2 s^{-1})	R_G (Å)	τ_G (ps)	D_G (10^{-6} cm^2 s^{-1})
				IN16B			
(CA1)	225	2.9(1)	400(70)	0.4(1)	2.7(1)	300(10)	0.4(1)
	250	2.7(1)	200(20)	0.6(1)	2.6(1)	300(30)	0.4(2)
				BASIS			
(CA2)	400	3.0(1)	8.2(1)	18(1)	3.3(3)	7.1(4)	26(4)
	500	3.4(1)	7.0(1)	27(1)	4.2(5)	6.5(4)	45(10)
	600	3.7(1)	7.1(1)	32(1)	5.9(3)	7.2(1)	80(15)
	700	5.2(1)	8.2(1)	55(1)	6.6(4)	7.8(2)	93(13)
(NAB)	400	3.1(1)	9.4(1)	17(1)	3.9(7)	7.9(8)	32(10)
	500	4.3(1)	6.6(1)	47(1)	4.8(7)	6.3(4)	61(20)
	600	4.2(1)	6.2(1)	47(2)	5.3(7)	5.8(3)	81(27)
	700	4.4(1)	5.9(1)	55(1)	7.2(9)	5.5(3)	157(55)

constant, D, through the relationship $D = R^2/n\tau$, where n = 2, 4, and 6 for diffusion in 1, 2, and 3 dimensions, respectively.[45,46] The dashed lines in Figure 4b are fits to a jump-diffusion model that assumes a Gaussian distribution of jump lengths

$$\Gamma_1(Q) = \frac{2\hbar}{\tau_G}\left(1 - \frac{\exp(Q^2\langle R_G^2\rangle}{6}\right) \quad (4)$$

where $\langle R_G^2\rangle$ is the mean square jump length. Free fits to the data yield jump distances of 2.7–2.9 Å and mean relaxation times of 0.2–0.4 ns for the Chudley–Elliott model and 2.6–2.7 Å and 0.2–0.3 ns for the Gaussian model. For any of the models, the corresponding diffusion constant D takes on values of approximately 0.4 × 10^{-6} cm^2 s^{-1}. The fit parameters for both models are shown in Table 2.

3.4. Quasielastic Spectra at High Temperatures. QENS measurements for the temperature range 400–700 K were performed on BASIS using the CA2 and NAB samples. These measurements targeted faster-time scale dynamics. Figure 5 shows $S_{meas}(Q, \omega)$ at 400 K and Q = 0.9 Å^{-1}, for both CA2 and NAB, whereas the spectra for 500, 600, and 700 K are shown in Figures S5 and S6. In agreement with the IN16B data on CA1, the higher-temperature spectra of CA2 and NAB can be approximated to a single Lorentzian and a linear, sloping, background; however, the here probed quasielastic component is now about 2 orders of magnitude broader as a result of the QENS signal dominated by faster-time scale dynamics. It should be noted that as a result of the broad nature of the quasielastic component, it is difficult to separate it from the background originating from even faster time scale dynamics and inelastic scattering contributions, such as vibrational motions. To obtain consistency between the fitted parameters, the offset of the background, $a(Q)$, (see eq 1) had to be adjusted and fixed manually for some of the temperatures and Q values; details are given in the captions of Figures S5 and S6.

As for CA1 as measured on IN16B, the Q dependence of the quasielastic width as extracted from the Lorentzian component, $\Gamma_1(Q)$, can be adequately described both by Chudley–Elliott and Gaussian jump diffusion models. For CA2 (Figure 6), free fits yield jump distances in the range 3.0–5.2 Å and mean residence times in the range 7.0–8.2 ps for the Chudley–Elliott model and 3.3–6.6 Å and 6.5–7.8 ps for the Gaussian model, respectively. For NAB (Figure 7), free fits yield jump distances in the range 3.1–4.4 Å and mean residence times in the range 5.9–9.4 ps for the Chudley–Elliott model and 3.9–7.2 Å and 5.5–7.9 ps for the Gaussian model, respectively. The parameters obtained from the two fits are thus overall similar (see Table 2). However, the Chudley–Elliot model is featured by a more consistent value of the jump length (4 Å), as well as a lower error, and the Gaussian model was fitted without considering the individual error from the data points (when the errors of the data points was considered for the Gaussian fit, the fit became extremely stiff and visibly ill

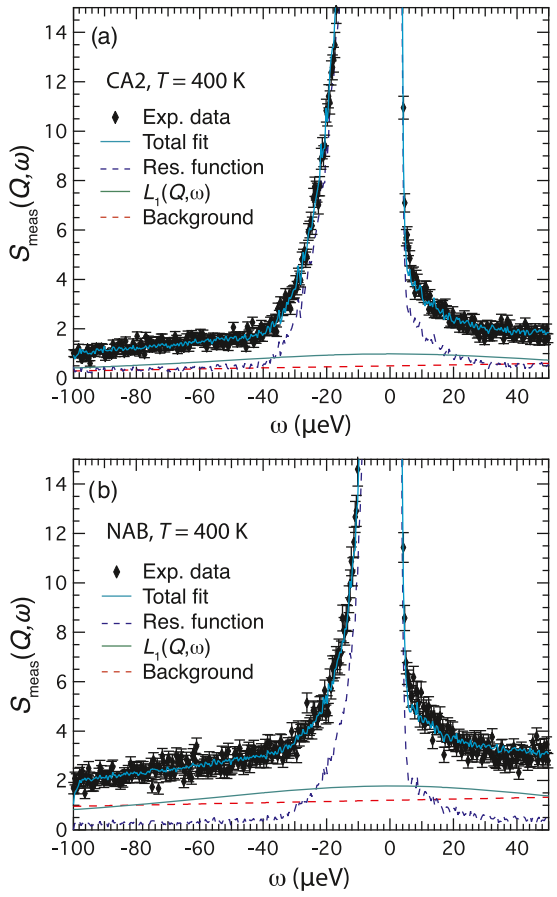

Figure 5. $S_{meas}(Q, \omega)$ of CA2 (a) and NAB (b) at Q = 0.9 Å^{-1} and 400 K, as measured on BASIS, together with their fits according to eq 1.

DOI: 10.1021/acs.jpcc.8b08451
J. Phys. Chem. C 2019, 123, 2019–2030

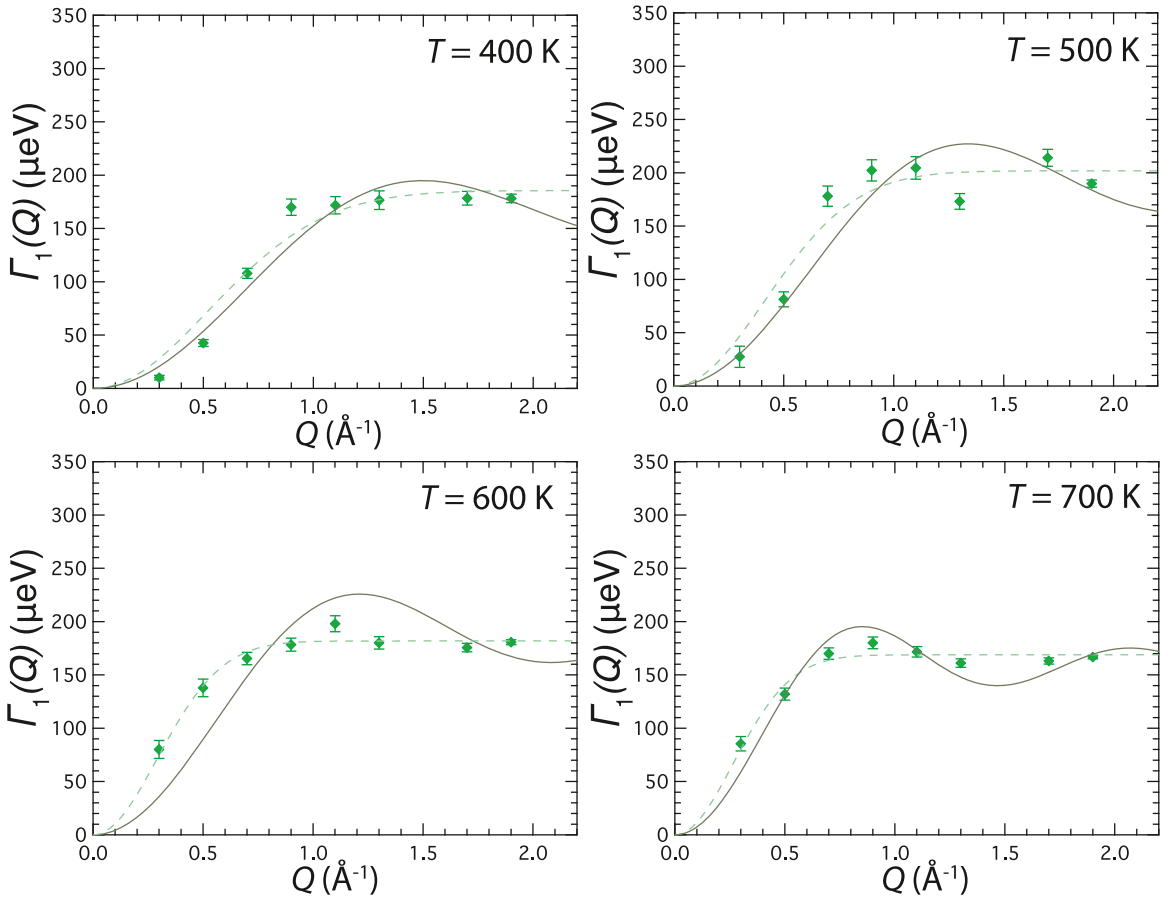

Figure 6. Q dependence of $\Gamma_1(Q)$ for CA2 as obtained from the BASIS data at 400, 500, 600, and 700 K. The solid lines are fits to a Chudley−Elliott model and the dashed lines are fits to a Gaussian model. The data point at Q = 1.5 Å^{-1} has been removed due to interference with a Bragg peak at 1.57 Å^{-1}.

fitting). Therefore, the Chudley−Elliot model is deemed to be most reliable for describing the observed dynamics.

Figure 8 compares the temperature dependence of the diffusion coefficient, D, for CA1, CA2, and NAB. The diffusion coefficient, rather than the mean residence time, τ, is shown here due to the fact that we observe not only a change in τ but a simultaneous change in the jump distances, R. Both CA2 and NAB show an Arrhenius dependence with an activation energy of 85(2) and 94(2) meV for the Chudley−Elliott model and 105(18) and 118(42) meV for the Gaussian model, for CA2 and NAB, respectively. The diffusion constants derived from the Chudley−Elliott model for CA1 are seemingly on the same trajectory as the Arrhenius dependence of the other two samples; however, with only two D values for CA1, any activation energy cannot be reliably determined.

3.5. Hydrogen Desorption at High Temperatures. NSE measurements within the temperature range 300−700 K were performed on the CA2 sample under ambient conditions with the specific aim to study the hydride-ion dynamics across the temperature range of hydrogen desorption. Figure 9 shows $I(Q, t)$ at a selection of temperatures between 400 and 660 K. The $I(Q, t)$s are generally featured by a low signal-to-noise ratio due to a low neutron polarization [the measured quantity in NSE and that relates directly to $I(Q, t)$] related to a low hydrogen concentration and/or an unfavorable ratio between coherent and incoherent scattering.[22] However, when comparing the $I(Q, t)$ at different temperatures, there is a noticeable change from no visible decay for temperatures between 400 and 525 K to a slight but significant decay for higher temperatures. Interestingly, the "threshold" temperature for dynamics as picked up in the experiment, i.e., around 550−600 K, coincides with a decrease in the incoherent scattering signal (Figure 10), which points toward some loss of hydrogen species from the sample. In comparison, the coherent scattering intensity, as relates primarily to Ba, Ti, and O (the coherent scattering from H is only about 0.9% of the total coherent scattering in CA2),[43] does not change with temperature, as expected considering that the hydrogen desorbs as H_2(g).

4. DISCUSSION

Our results from the low- and high-temperature neutron backscattering experiments and the NSE spectroscopy experiment on $BaTiO_{3-x}H_x$ reveal new insights into hydrogen dynamics in perovskite-type materials, now stretching from protic to hydridic species. Analyses of the QENS spectra measured at low (225 and 250 K) and high (400−700 K) temperatures show that the observed dynamics can be adequately described by established models of jump diffusion, with a preference for the Chudley−Elliott model.

At low temperatures, ≤250 K, all of the models feature a jump distance of about 2.8 Å, which, crucially, matches the distance of the nearest neighboring (NN) O/H atoms or oxygen vacancies in $BaTiO_{3-x}H_x$ of approximately 2.8 Å (Figure 11), with a mean residence time of the order of 0.1 ns (Table 2). These results are therefore consistent with hopping

DOI: 10.1021/acs.jpcc.8b08451
J. Phys. Chem. C 2019, 123, 2019−2030

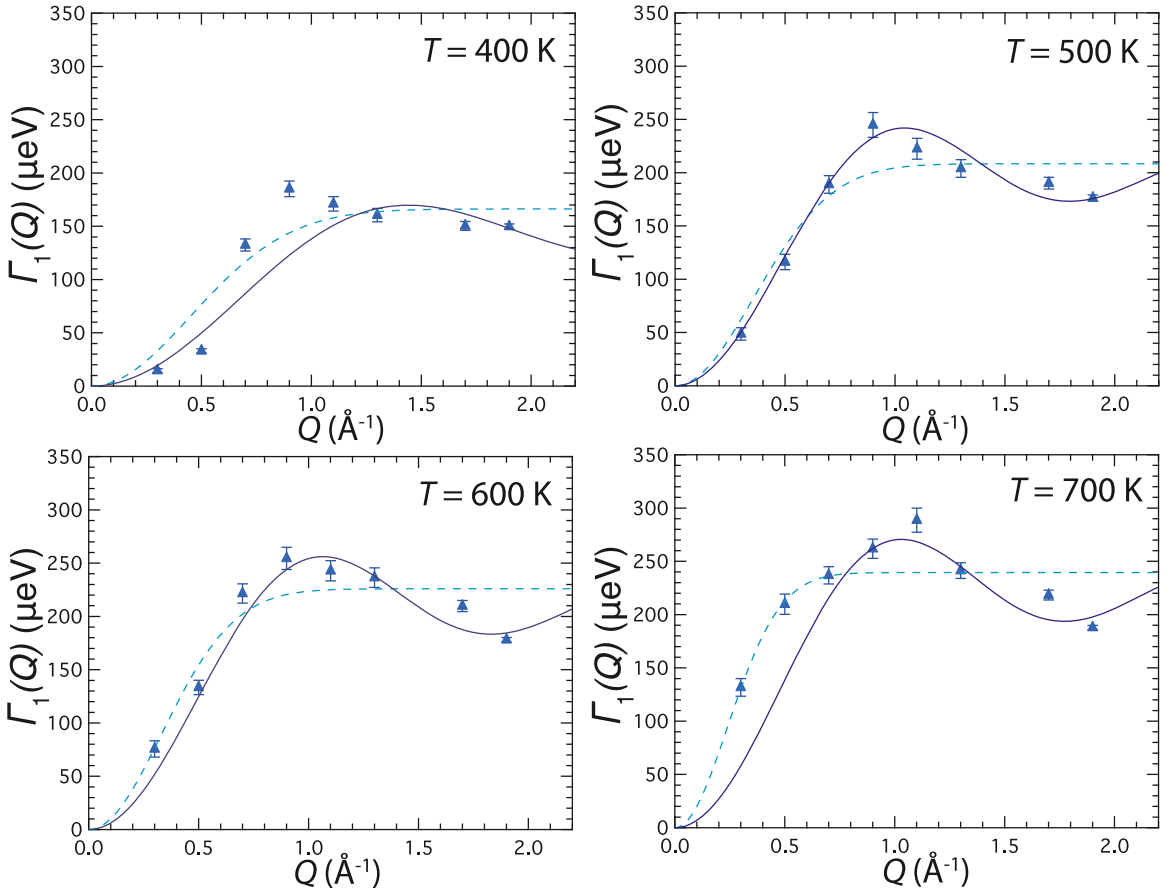

Figure 7. Q dependence of $\Gamma_1(Q)$ for NAB, as obtained from the BASIS data at 400, 500, 600, and 700 K. The solid lines are fits to a Chudley–Elliott model and the dashed lines are fits to a Gaussian model. The data point at Q = 1.5 Å^{-1} has been removed due to interference with a Bragg peak at 1.57 Å^{-1}.

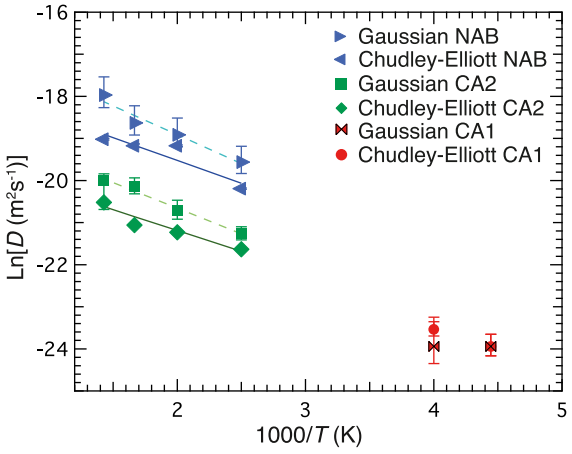

Figure 8. Arrhenius plot of the diffusion coefficient D, extracted from the Chudley–Elliott and Gaussian models fitted to the IN16B and BASIS data of the CA1, CA2, and NAB samples. The fits correspond to activation energies of 85(2) and 94(2) meV for the Chudely–Elliot model and 105(18) and 118(42) meV for the Gaussian model for CA2 and NAB, respectively. The pre-exponential factor, D_0, in the Arrhenius law corresponds to 2.0 × 10^{-4} and 2.9 × 10^{-4} cm^2 s^{-1} for the Chudely–Elliot model and 5.5 × 10^{-4} and 9.5 × 10^{-4} cm^2 s^{-1} for the Gaussian model for CA2 and NAB, respectively. The data points of CA2 have been vertically shifted by −1.5, for easier comparison between the different data sets.

of hydride ions, constrained by the perovskite lattice, between vacant sites of the corners of the same or neighboring Ti(O/H)$_{6-\delta}$ polyhedra, where δ reflects the amount of oxygen vacancies. Crucially, this time scale is much shorter than what would be detected for oxygen diffusion at equivalent temperatures. This latter feature indicates that the hydride-ion hopping is not dependent on the counter diffusion of oxygen ions but rather points toward a mechanism in which the hydride ions jump to neighboring oxygen vacancy sites in the perovskite structure. Indeed, CA1 contains a significant concentration of oxygen vacancies, cf. Table 1, which thus might enable the formation of percolating pathways of oxygen vacancies in the perovskite lattice. In principle, the hydride ions may, in the case of a large hydride-ion concentration ($x \geq 0.4$) as well, diffuse in the structure through percolating pathways of hydride ions, even for a very low oxygen vacancy concentration.[3] However, as the hydride-ion concentration in CA1 is only x = 0.10, the latter process is rather unlikely to happen. The important role of oxygen vacancies for hydride-ion diffusion is further reflected by the NSE data, which show the onset of hydride-ion dynamics at around the hydrogen desorption temperature. This is in accordance with an increased amount of oxygen vacancies and thus higher hydride-ion mobility in the perovskite structure.

At higher temperatures, ≥400 K, the jump distances increase from a value of 3.0 Å (for CA2) and 3.1 Å (for NAB) at 400 K to a value between 3.4 and 4.4 Å between 500 and 700 K and with a mean residence time of the order of picoseconds and an

DOI: 10.1021/acs.jpcc.8b08451
J. Phys. Chem. C 2019, 123, 2019−2030

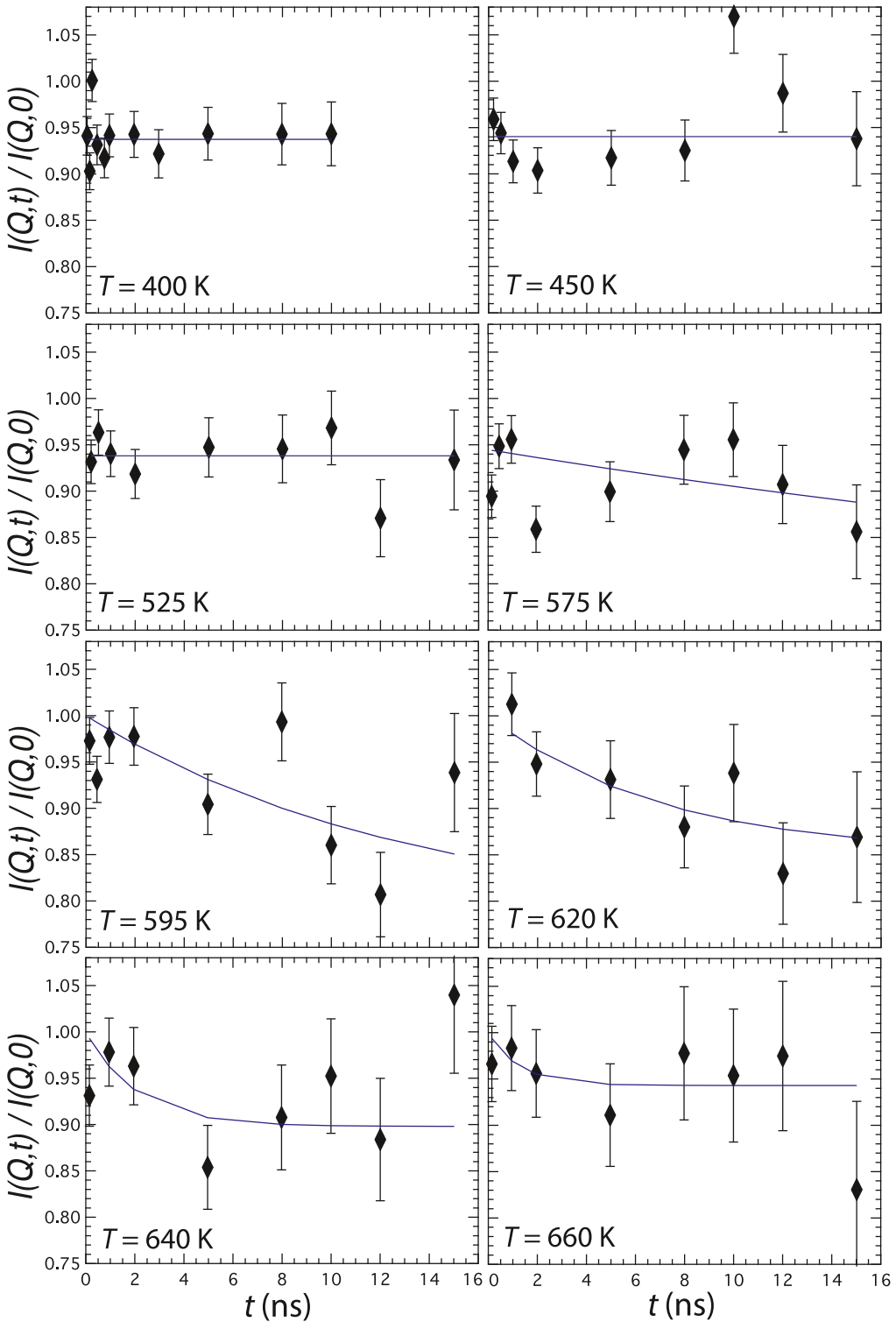

Figure 9. $I(Q, t)$ for CA2, as extracted from the NSE measurements at $Q = 1.1$ Å^{-1}. Note the slight but significant decay of $I(Q, t)$ for temperatures above 550 K, which occurs in conjunction with loss of hydride ions (incoherent scattering), cf. Figure 10. Lines are guides to the eyes.

activation energy $E_a \approx 0.1$ eV. Therefore, at 400 K, the jump distance is, similar to that of CA1 at low temperatures (225 and 250 K), close to NN jumps, whereas at >400 K, it is of the order of the distance between second nearest neighboring (2NN) oxygen vacancies (Figure 11). The jump distance at the highest temperatures is thus in agreement with the recent gaseous hydrogen exchange experiments on $BaTiO_{3-x}H_x$ and the similar compound $LaSrCoO_3H_{0.7}$ by Tang et al.,[18] who found that the hydride-ion transport relies on 2NN jumps at temperatures between 600 and 1000 K. However, the activation energy E_a, as reported by Tang et al.,[18] in the range of 2−2.5 eV, is considerably higher than the value of ≈0.1 eV, as derived from our experiments. This discrepancy may be related to the fact that while QENS yields the pure bulk self-diffusion coefficient of hydride ions, the gaseous hydrogen exchange experiments conducted by Tang et al.[18]

DOI: 10.1021/acs.jpcc.8b08451
J. Phys. Chem. C 2019, 123, 2019−2030

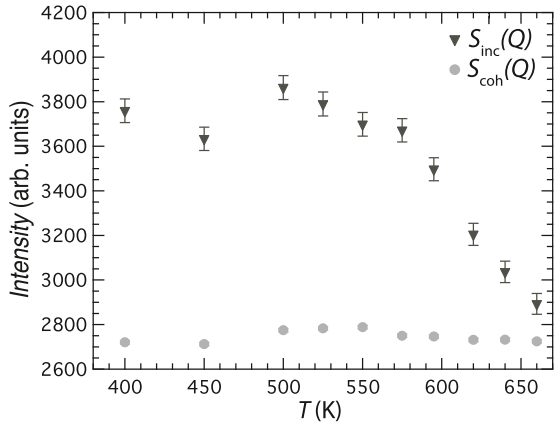

Figure 10. Temperature dependence of the coherent and incoherent scattering intensities for CA2, as extracted from the neutron polarization analysis at Q = 1.1 Å^{-1}. The data points of $S_{coh}(Q)$ have been vertically shifted by +2000 for easier comparison.

measure a chemical diffusion coefficient, as it depends on the chemical potential between the gas and solid phase, which will as well be determined by surface effects and grain boundaries in the material. The higher E_a, as found by Tang et al.,[18] is rather comparable to the ones found for oxygen diffusion in $BaTiO_3$ (cf. $E_a \approx 2-2.8$ eV[47−52]), pointing toward a hydride-ion conduction mechanism dependent on the simultaneous movement of oxygen ions. In comparison, Bridges et al.,[21] in their QENS experiment on $LaSrCoO_3H_{0.7}$, reported an E_a of around 0.2 eV. Tang et al.[18] argued that the hydride-ion diffusion in $LaSrCoO_3H_{0.7}$ occurs during hydrogen desorption (and thus the creation of oxygen vacancies) and hence shows a heavily reduced E_a as compared to the one extracted from the gaseous hydrogen exchange experiments. In our case, we observe significant hydride-ion jump dynamics well below the hydrogen desorption temperature, as well as for x significantly lower than 0.4. In view of the results reported by Tang et al.,[18] it follows that the high amount of oxygen vacancies in CA2 and NAB seems to enable the jump diffusion dynamics of hydride ions at a much lower temperature than the hydrogen release temperature and with a significantly lower activation energy. Such an oxygen vacancy-assisted hydride-ion conduction mechanism is further supported by the somewhat shorter mean residence times observed for the NAB sample, containing more oxygen vacancies, compared to that in CA2 (cf. Table 2). This is also in agreement with the NSE data showing an onset of dynamics at around the hydrogen desorption temperature, which is congruent with an increased amount of oxygen vacancies and thus higher hydride-ion mobility in the perovskite structure. These results are in accordance with recent first-principles calculations for $BaTiO_{3-x}H_x$, which show a low activation energy (0.28 eV) of vacancy-assisted diffusional motion,[16] as well as with results obtained from anion exchange studies[12,19] and ionic conductivity measurements[53] that show that the diffusional motion of the hydride ions can be even more promoted by introducing oxygen vacancies.

It should be noted, however, that it is at present not clear whether the hydride ions maintain their negative charge during the diffusion process or if the diffusion involves the transformation into a proton followed by interstitial diffusion. Results from computer simulations show that E_a for interstitial diffusion of protons in $BaTiO_3$ takes on a value of ca. 0.2 eV,[15] whereas results from QENS studies of acceptor-doped perovskite materials, supported by computational techniques, show activation energies typically in the range 0.1−0.2 eV for diffusional motions of protons,[22−26,54−56] thus being quite comparable to our results. Nonetheless, since we observe no protonic state in the NMR spectra, such a $H^- \rightarrow H^+ \rightarrow H^-$ transformation diffusion mechanism is not supported by any experimental data reported so far.

5. CONCLUSIONS

We studied the dynamics of hydride ions in three metal-hydride-reduced $BaTiO_{3-x}H_x$ samples, with varying hydride-ion and oxygen vacancy concentrations. The elastic intensity as a function of increasing temperature evolves from being essentially linear at low temperatures (≈2−200 K) to a nonlinear regime between ≈200 and 550 K, thus reflecting the transition from dynamics associated with purely harmonic vibrational motions to diffusional hydride-ion motions accessible with the used QENS spectrometers. Quasielastic spectra measured in the low-temperature region (225 and 250 K) reveal dynamics associated with hydride-ion jumps between nearest neighbor oxygen vacancies with a mean residence time of the order of 0.1 ns. Quasielastic spectra measured at higher temperatures (>400 K) reveal dynamics associated with hydride-ion jumps between next-nearest neighboring oxygen vacancies with a mean residence time of the order of picoseconds, with no strong dependence on the concentration of hydride ions and oxygen vacancies. The obtained hydride-ion diffusion coefficients derived from QENS at low temperature were in the range $D = (0.4-0.6) \times 10^{-6}$ cm^2 s^{-1} between 225 and 250 K. At higher temperatures, D increases from about 18×10^{-6} cm^2 s^{-1} at 400 K to 55×10^{-6} cm^2 s^{-1} at 700 K. Activation energies E_a were derived from the measurements at high temperatures and take on values of about 0.1 eV and show a slight increase with increasing oxygen vacancy concentration. This is useful new data for the comparison with future experimental and computational results and thus motivates further efforts to determine the defect nature and

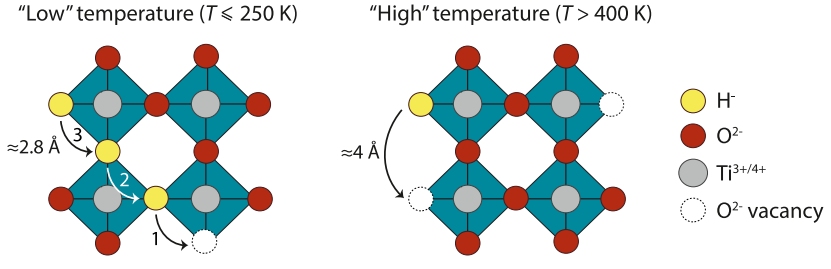

Figure 11. Schematic illustration of the observed hydride-ion dynamics at low (≤250 K) and high (≥400 K) temperatures, respectively.

DOI: 10.1021/acs.jpcc.8b08451
J. Phys. Chem. C 2019, 123, 2019−2030

transport properties of metal hydride-reduced $BaTiO_3$ materials.

■ ASSOCIATED CONTENT

Supporting Information

The Supporting Information is available free of charge on the ACS Publications website at DOI: 10.1021/acs.jpcc.8b08451.

Photograph of an oxyhydride sample, Rietvelt refinements for all samples, NMR results for CA2, the complete set of $S_{meas}(Q, \omega)$ for all samples at all measured temperatures, and all author names of refs 3, 11−13 (PDF)

■ AUTHOR INFORMATION

Corresponding Author

*E-mail: maths.karlsson@chalmers.se.

ORCID

Ulrich Häussermann: 0000-0003-2001-4410
Andrew J. Pell: 0000-0002-2542-8113
Niina H. Jalarvo: 0000-0003-0644-6866
Maths Karlsson: 0000-0002-2914-6332

Notes

The authors declare no competing financial interest.

■ ACKNOWLEDGMENTS

This research was funded by the Swedish Foundation for Strategic Research (grant no. ICA10-0001) and the Swedish Research Council (grant nos. 2014-3980 and 2016-03441). The ILL and NCNR are acknowledged for access to neutron beam facilities and access to the HFBS and Neutron Spin-Echo Spectrometers, as provided by the Center for high-resolution neutron scattering, a partnership between the National Science Foundation and NIST under agreement no. DMR-1508249. The research at Oak Ridge National Laboratory of the Spallation Neutron Source was sponsored by the Scientific User Facilities Division, Office of Basic Energy Sciences, U.S. Department of Energy. The spectrometer BASIS is supported by the Jülich Center for Neutron Science (JCNS), Germany, via the partner user program.

■ REFERENCES

(1) Romero, F. D.; Leach, A.; Möller, A.; Foronda, F.; Blundell, S.; Hayward, M. Strontium Vanadium Oxide-Hydrides: "Square-Planar" Two-Electron Phases. *Angew. Chem., Int. Ed.* **2014**, *53*, 7556−7559.

(2) Tassel, C.; Goto, Y.; Kuno, Y.; Hester, J.; Green, M.; Kobayashi, Y.; Kageyama, H. Direct Synthesis of Chromium Perovskite Oxyhydride with a High Magnetic-Transition Temperature. *Angew. Chem., Int. Ed.* **2014**, *53*, 10377−10380.

(3) Kobayashi, Y.; Hernandez, O. J.; Sakaguchi, T.; Yajima, T.; Roisnel, T.; Tsujimoto, Y.; Morita, M.; Noda, Y.; Mogami, Y.; Kitada, A.; et al. An Oxyhydride of $BaTiO_3$ Exhibiting Hydride Exchange and Electronic Conductivity. *Nat. Mater.* **2012**, *11*, 507−511.

(4) Malaman, B.; Brice, J. F. Etude Structurale de l'Hydruro-Oxyde LaHO par Diffraction des Rayons X et par Diffraction des Neutrons. *J. Solid State Chem.* **1984**, *53*, 44−54.

(5) Clark, N. J.; Wu, E. Hydrogen Absorption by M5X3 Phase Zr-Al Compounds. *J. Less-Common Met.* **1988**, *142*, 145−154.

(6) Huang, B.; Corbett, J. D. Ba_3AlO_4H: Synthesis and Structure of a New Hydrogen-Stabilized Phase. *J. Solid State Chem.* **1998**, *141*, 570−575.

(7) Huang, B.; Corbett, J. D. $Ba_{21}Ge_2O_5H_{24}$ and Related Phases. A Corrected Structure Type and Composition for a Zintl Phase Stabilized by Hydrogen. *Inorg. Chem.* **1998**, *37*, 1892−1899.

(8) Hayashi, K.; Matsuishi, S.; Kamiya, T.; Hirano, M.; Hosono, H. Light-Induced Conversion of an Insulating Refractory Oxide Into a Persistent Electronic Conductor. *Nature* **2002**, *419*, 462−465.

(9) Hayward, M. A.; Cussen, E. J.; Claridge, J. B.; Bieringer, M.; Rosseinsky, M. J.; Kiely, C. J.; Blundell, S. J.; Marshall, I. M.; Pratt, F. L. The Hydride Anion in an Extended Transition Metal Oxide Array: $LaSrCoO_3H_{0.7}$. *Science* **2002**, *295*, 1882−1884.

(10) Helps, R. M.; Rees, N. H.; Hayward, M. A. $Sr_3Co_2O_{4.33}H_{0.84}$: An Extended Transition Metal Oxide-Hydride. *Inorg. Chem.* **2010**, *49*, 11062−11068.

(11) Yajima, T.; Takeiri, F.; Aidzu, K.; Akamatsu, H.; Fujita, K.; Yoshimune, W.; Ohkura, M.; Lei, S.; Gopalan, V.; Tanaka, K.; et al. A Labile Hydride Strategy for the Synthesis of Heavily Nitridized $BaTiO_3$. *Nat. Chem.* **2015**, *7*, 1017−1023.

(12) Mikita, R.; Aharen, T.; Yamamoto, T.; Takeiri, F.; Ya, T.; Yoshimune, W.; Fujita, K.; Yoshida, S.; Tanaka, K.; Batuk, D.; et al. Topochemical Nitridation with Anion Vacancy-Assisted N^{3-}/O^{2-} Exchange. *J. Am. Chem. Soc.* **2016**, *138*, 3211−3217.

(13) Masuda, N.; Kobayashi, Y.; Hernandez, O.; Bataille, T.; Paofai, S.; Suzuki, H.; Ritter, C.; Ichijo, N.; Noda, Y.; Takegoshi, K.; et al. Hydride in $BaTiO_{2.5}H_{0.5}$: A Labile Ligand in Solid State Chemistry. *J. Am. Chem. Soc.* **2015**, *137*, 15315−15321.

(14) Iwazaki, Y.; Suzuki, T.; Tsuneyuki, S. Negatively Charged Hydrogen at Oxygen-Vacancy Sites in $BaTiO_3$: Density-Functional Calculation. *J. Appl. Phys.* **2010**, *108*, No. 083705.

(15) Zhang, J.; Gou, G.; Pan, B. Study of Phase Stability and Hydride Diffusion Mechanism of $BaTiO_3$ Oxyhydride From First-Principles. *J. Phys. Chem. C* **2014**, *118*, 17254−17259.

(16) Liu, X.; Bjørheim, T.; Haugsrud, R. Formation and Migration of Hydride Ions in $BaTiO_{3-x}H_x$ Oxyhydride. *J. Mater. Chem. A* **2017**, *5*, 1050−1056.

(17) Ito, T.; Koda, A.; Shimomura, K.; Higemoto, W.; Matsuzaki, T.; Kobayashi, Y.; Kageyama, H. Excited Configurations of Hydrogen in the $BaTiO_{3-x}H_x$ Perovskite Lattice Associated with Hydrogen Exchange and Transport. *Phys. Rev. B* **2017**, *95*, No. 020301.

(18) Tang, Y.; Kobayashi, Y.; Shitara, K.; Konishi, A.; Kuwabara, A.; Nakashima, T.; Tassel, C.; Yamamoto, T.; Kageyama, H. On Hydride Diffusion in Transition Metal Perovskite Oxyhydrides Investigated via Deuterium Exchange. *Chem. Mater.* **2017**, *29*, 8187−8194.

(19) Takeiri, F.; Aidzu, K.; Yajima, T.; Matsui, T.; Yamamoto, T.; Kobayashi, Y.; Hester, J.; Kageyama, H. Promoted Hydride/Oxide Exchange in $SrTiO_3$ by Introduction of Anion Vacancy via Aliovalent Cation Substitution. *Inorg. Chem.* **2017**, *56*, 13035−13040.

(20) Nedumkandathil, R.; Jaworski, A.; Grins, J.; Bernin, D.; Karlsson, M.; Eklöf-Österberg, C.; Neagu, A.; Tai, C.-W.; Pell, A. J.; Häussermann, U. Hydride Reduction of $BaTiO_3$ - Oxyhydride Versus O Vacancy Formation. *ACS Omega* **2018**, *3*, 11426−11438.

(21) Bridges, C. A.; Fernandez-Alonso, F.; Goff, J. P.; Rosseinsky, M. J. Observation of Hydride Mobility in the Transition-Metal Oxide Hydride $LaSrCoO_3H_{0.7}$. *Adv. Mater.* **2006**, *18*, 3304−3308.

(22) Karlsson, M. Proton Dynamics in Oxides: Insight Into the Mechanics of Proton Conduction From Quasielastic Neutron Scattering. *Phys. Chem. Chem. Phys.* **2015**, *17*, 26−38.

(23) Noferini, D.; Koza, M. M.; Fouquet, P.; Nilsen, G. J.; Kemei, M. C.; Rahman, S. M. H.; Maccarini, M.; Eriksson, S.; Karlsson, M. Proton Dynamics in Hydrated $BaZr_{0.9}M_{0.1}O_{2.95}$ (M = Y and Sc) Investigated with Neutron Spin-Echo. *J. Phys. Chem. C* **2016**, *120*, 13963−13969.

(24) Noferini, D.; Koza, M. M.; Karlsson, M. Localized Proton Motions in Acceptor-Doped Barium Zirconates. *J. Phys. Chem. C* **2017**, *121*, 7088−7093.

(25) Noferini, D.; Koza, M. M.; Rahman, S. M. H.; Evenson, Z.; Nilsen, G. J.; Eriksson, S.; Wildes, A. R.; Karlsson, M. Role of the Doping Level in Localized Proton Motions in Acceptor-Doped Barium Zirconate Proton Conductors. *Phys. Chem. Chem. Phys.* **2018**, *20*, 13697−13704.

(26) Noferini, D.; Frick, B.; Koza, M. M.; Karlsson, M. Proton Jump Diffusion Dynamics in Hydrated Barium Zirconates Studied by High-

DOI: 10.1021/acs.jpcc.8b08451
J. Phys. Chem. C 2019, 123, 2019−2030

Resolution Neutron Backscattering Spectroscopy. *J. Mater. Chem. A* **2018**, *6*, 7538−7546.
(27) The mention of all commercial suppliers in this paper is for clarity and does not imply the recommendation or endorsement of these suppliers by NIST.
(28) Rodríguez-Carvajal, J. *Abstracts of the Satellite Meeting on Powder Diffraction of the XV IUCr Congress*; Toulouse: France, 1990; p 127.
(29) Hwang, T.-L.; Van Zijl, P.; Garwood, M. Fast Broadband Inversion by Adiabatic Pulses. *J. Magn. Reson.* **1998**, *133*, 200−203.
(30) Kervern, G.; Pintacuda, G.; Emsley, L. Fast Adiabatic Pulses for Solid-State NMR of Paramagnetic Systems. *Chem. Phys. Lett.* **2007**, *435*, 157−162.
(31) Pell, A. J.; Pintacuda, G. Broadband Solid-State MAS NMR of Paramagnetic Systems. *Prog. Nucl. Magn. Reson. Spectrosc.* **2015**, *84*−*85*, 33−72.
(32) Frick, B.; Mamontov, E.; Eijck, L. V.; Seydel, T. Recent Backscattering Instrument Developments at the ILL and SNS. *Phys. Chem.* **2010**, *224*, 33−60.
(33) https://www.ill.eu/users/instruments/instruments-list/in16b/description/instrument-layout/ (accessed May 16, 2018).
(34) Meyer, A.; Dimeo, R. M.; Gehring, P. M.; Neumann, D. A. The High-Flux Backscattering Spectrometer at the NIST Center for Neutron Research. *Rev. Sci. Instrum.* **2003**, *74*, 2759−2777.
(35) Mamontov, E.; Herwig, K. W. A Time-Of-Flight Backscattering Spectrometer at the Spallation Neutron Source, BASIS. *Rev. Sci. Instrum.* **2011**, *82*, No. 085109.
(36) Experiment number: DOI: 10.5291/ILL-DATA.7-03-148.
(37) Azuah, R.; Kneller, L.; Qiu, Y.; Tregenna-Piggott, P. L. W.; Brown, C.; Copley, J.; Dimeo, R. DAVE: A Comprehensive Software Suite for the Reduction, Visualization, and Analysis of Low Energy Neutron Spectroscopic Data. *J. Res. Natl. Inst. Stand. Technol.* **2009**, *114*, 341−358.
(38) Rosov, N.; Rathgeber, S.; Monkenbusch, M. *Scattering from Polymers: Characterization by X-rays, Neutrons, and Light*; Cebe, P., Hsaio, B. S., Lohse, D. J., Eds.; ACS Symposium Series 739; American Chemical Society: Washington DC, 2000; pp 103−116.
(39) Udovic, T. J.; Verdal, N.; Rush, J. J.; Vries, D. J. D.; Hartman, M. R.; Vajo, J. J.; Gross, A. F.; Skripov, A. V. Mapping Trends in the Reorientational Mobilities of Tetrahydroborate Anions via Neutron-Scattering Fixed-Window Scans. *J. Alloys Compd.* **2013**, *580*, S47−S50.
(40) Frick, B. Neutron Backscattering. In *Neutron and X-ray Spectroscopy*; Hodeau, J. L., Hippert, F., Geissler, E., vre-Berna, E., Regnard, J.-R., Eds.; Springer: Netherlands, 2006; pp 483−527.
(41) Tang, W. S.; Dimitrievska, M.; Chotard, J.-N.; Zhou, W.; Janot, R.; Skripov, A. V.; Udovic, T. J. Structural and Dynamical Trends in Alkali-Metal Silanides Characterized by Neutron-Scattering Methods. *J. Phys. Chem. C* **2016**, *120*, 21218−21227.
(42) Song, C.-R.; Yoo, H.-I. Chemical Diffusivity of $BaTiO_{3-\delta}$ I. Experimental determination. *Solid State Ionics* **1999**, *120*, 141−153.
(43) Neutron Scattering Lengths and Cross Sections at the NIST Center for Neutron Research, 2018. https://www.ncnr.nist.gov/resources/n-lengths/ (accessed May 16, 2018).
(44) Bée, M. *Quasielastic Neutron Scattering*; Millen, D. J., Ed.; IOP Publishing: Bristol, 1988.
(45) Hempelmann, R. *Quasielastic Neutron Scattering and Solid State Diffusion*; Clarendon Press: Oxford, 2000.
(46) Alvine, K. J.; Tyagi, M.; Brown, C. M.; Udovic, T. J.; Jenkins, T.; Pitman, S. G. Hydrogen Species Motion in Piezoelectrics: A Quasi-Elastic Neutron Scattering Study. *J. Appl. Phys.* **2012**, *111*, No. 053505.
(47) Preis, W.; Sitte, W. Electronic Conductivity and Chemical Diffusion in n-Conducting Barium Titanate Ceramics at High Temperatures. *Solid State Ionics* **2006**, *177*, 3093−3098.
(48) Wernicke, R. Kinetics of Equilibrium Restoration in Barium Titanate Ceramics. *Philips Res. Rep.* **1976**, *31*, 526−543.
(49) Nowotny, J.; Rekas, M. Defect Structure, Electrical Properties and Transport in Barium Titanate. VII. Chemical Diffusion in Nb-Doped $BaTiO_3$. *Ceram. Int.* **1994**, *20*, 265−275.
(50) Preis, W. Chemical Diffusion and Defect Chemistry of Grain Boundaries in n-Type Barium Titanate Ceramics. *Solid State Ionics* **2017**, *299*, 82−88.
(51) Maier, J.; Schwitzgebel, G.; Hagemann, H.-J. Electrochemical Investigations of Conductivity and Chemical Diffusion in Pure and Doped Cubic $SrTiO_3$ and $BaTiO_3$. *J. Solid State Chem.* **1985**, *58*, 1−13.
(52) Kolodiazhnyi, T.; Petric, A. Effect of P_{O_2} on Bulk and Grain Boundary Resistance of n-Type $BaTiO_3$ at Cryogenic Temperatures. *J. Am. Ceram. Soc.* **2003**, *86*, 1554−1559.
(53) Kobayashi, G.; Hinuma, Y.; Matsuoka, S.; Watanabe, A.; Iqbal, M.; Hirayama, M.; Yonemura, M.; Kamiyama, T.; Tanaka, I.; Kanno, R. Pure H^- Conduction in Oxyhydrides. *Science* **2016**, *351*, 1314−1317.
(54) Dawson, J. A.; Miller, J. A.; Tanaka, I. First-Principles Insight Into the Hydration Ability and Proton Conduction of the Solid State Proton Conductor, Y and Sn Co-doped $BaZrO_3$. *Chem. Mater.* **2015**, *27*, 901−908.
(55) Björketun, M. E.; Sundell, P. G.; Wahnström, G. Effect of Acceptor Dopants on the Proton Mobility in $BaZrO_3$: A Density Functional Investigation. *Phys. Rev. B* **2007**, *76*, No. 054307.
(56) Jing, Y.; Matsumoto, H.; Aluru, N. R. Mechanistic Insights into Hydration of Solid Oxides. *Chem. Mater.* **2018**, *30*, 138−144.

DOI: 10.1021/acs.jpcc.8b08451
J. Phys. Chem. C 2019, 123, 2019−2030